particles

Review

Cosmic Ray Muon Navigation for Subsurface Environments: Technologies and Challenges

Dongqing Zhao [1,2,*], Pengfei Li [2] and Linyang Li [2]

[1] Key Laboratory of Smart Earth, No. 66, Minzuyuan Road, Beijing 100094, China
[2] School of Geospatial Information, Information Engineering University, No. 62, Kexue Road, Zhengzhou 450001, China; abc13933787600lpf@163.com (P.L.); linyangli@whu.edu.cn (L.L.)
* Correspondence: dongqing.zhao@hotmail.com

Abstract: The global navigation satellite system (GNSS), using electromagnetic signals, enables continuous positioning throughout the entire surface of the Earth. However, underwater and underground environments significantly restrict the propagation of electromagnetic waves. The sole approach to aid positioning is the utilization of sound signals. Signal blockage in underground and indoor environments demands the accurate location of anchor points for local positioning, which requires previous deployment. Unlike radio waves, the cosmic ray muons are highly reliable natural signal sources for positioning, remaining immune to spoofing and interference. Starting from the standpoint of navigation and positioning, this paper briefly introduces the physical properties of cosmic ray muons and outlines the measurements and positioning principles of muon navigation, including trilateral localization based on the time of flight (TOF) and angular localization based on the angle of arrival (AOA). It subsequently presents the pertinent studies conducted and analyzes the findings. Finally, the challenges of muon navigation are explored from three perspectives: positioning signals, positioning models, and application scenarios. This will offer some new ideas for the domain of localization for further research on muon positioning.

Keywords: cosmic ray muons; muon measurements; muon navigation; time of flight (TOF); angle of arrival (AOA)

Academic Editor: Armen Sedrakian

Received: 10 March 2025
Revised: 6 April 2025
Accepted: 16 April 2025
Published: 22 April 2025

Citation: Zhao, D.; Li, P.; Li, L. Cosmic Ray Muon Navigation for Subsurface Environments: Technologies and Challenges. *Particles* **2025**, *8*, 46. https://doi.org/10.3390/particles8020046

1. Introduction

The global navigation satellite system (GNSS) is the most widely used positioning, navigation, and timing (PNT) technology. However, radio signals are easily blocked and jammed, and they cannot penetrate buildings and water. It is only possible to locate in indoors, underground, and underwater environments with the aid of other techniques such as inertial measurement unit (IMU) [1], acoustics [2], ultra wideband (UWB) [3], vision [4], Wi-Fi or 4G/5G [5], geomagnetism [6], gravity [7], and so on. The marine environment generally employs a combination of the GNSS and the acoustic positioning system [8], predominantly utilizing long baseline (LBL), short baseline (SBL), and ultra-short baseline (USBL) techniques. The complexity and variety of the marine environment, in contrast to the atmosphere, including variations in salinity, temperature, and density, render acoustic wave pathways unpredictable. Particularly in shallow coastal depths, acoustic wave propagation is also severely limited by solar radiation, seasonal cycles, the mixing of water due to currents, and rivers or wastewater. A single sensor's lack of adaptability prevents it from meeting ubiquitous localization requirements. Multiple sensor fusion positioning is used to improve the location accuracy in different scenarios. Frequently used combinations include GNSS/INS [9], Vision/INS [10], INS/DVL [11], vision/geomagnetism/5G [12], and so on. This research aims to develop a smarter, more integrated, and ubiquitously comprehensive PNT system that works indoors/outdoors, aboveground/underground, and above water/underwater [13].

Particles and nuclei from celestial bodies, such as supernovae, strike the Earth and other planets. Due to their extreme energy, these primary cosmic rays interact with the atmosphere through a series of nuclear processes, resulting in the formation of many particle clusters. Galactic cosmic rays, predominantly composed of protons, interact with the Earth's atmosphere to generate secondary particles, including muons. When these high-energy protons collide with atmospheric nuclei, they initiate cascades of secondary particles such as pions and kaons, which subsequently decay into muons. This natural process contributes significantly to the population of muons observed at the Earth's surface. After colliding with the Earth's atmosphere, these high-energy protons form π mesons, which then decay into muons and neutrinos. Cosmic ray muons can be used in geophysics to detect the internal structure of volcanoes [14–16], predict volcanic eruptions [17,18], monitor tidal movements [19], scan nuclear material [20], synchronize time [21,22], and even detect structures inside some buildings, like the pyramids [23], the tomb of Qin Shi Huang [24], and the ancient city walls of Xi'an [25]. In addition to these cosmic sources, muons can also be produced by manmade accelerators. These facilities accelerate protons to high energies and direct them toward specific targets, resulting in particle interactions that similarly produce muons. The fundamental sciences, including materials science, chemistry, biology, and nuclear physics, are the principal fields that use accelerator-produced muons.

In contrast to GNSS radio signals, cosmic ray muons possess significant penetrating power and exhibit relativistic characteristics, making them suitable for ubiquitous PNT [26]. Cosmic ray muons impact the Earth's surface, and unlike radio waves—which are susceptible to interference from both natural and manmade sources—these high-energy particles can penetrate deeply into the Earth's subsurface. Consequently, they work well in enclosed settings, including indoor, subterranean, and underwater. In 2020, Hiroyuki Tanaka, a scholar at the University of Tokyo, first proposed the concept of muon navigation [27] and carried out a series of experiments [28–31]. Other scholars also conducted studies on this foundation [32–35], introducing muon navigation technology to the public.

This novel technique originated in the field of high-energy particles, where navigation practitioners were not well-versed in cosmic ray muons. This survey article presents the basic concepts of muon navigation from the standpoint of PNT. Its objectives are to deepen our grasp of the muon positioning mechanism, enhance our understanding of cosmic ray muons, assess positioning errors, and promote the usage of muon navigation. This manuscript makes the following main contributions:

(1) Some physical properties of cosmic ray muons are sorted out, focusing on the observed flux results and energy-loss models. These penetration metrics can be used to evaluate the availability of muon navigation and determine in which scenarios using it is appropriate.

(2) The necessary measurements for muon navigation are summarized, including the time of flight (TOF) and incident coordinates. The TOF can be directly converted to distance for trilateral resection. With the incidence coordinates of each layer, it is possible to calculate the incidence angle and perform angle of arrival (AOA) positioning. These are the basic observables for localization and provide the basis for subsequent research on the principles of muon positioning.

(3) We present the basic principles of muon navigation and related achievements. The challenges faced are also analyzed in terms of navigation signals, positioning models, and application scenarios. This provides a valuable reference for further extensive muon navigation research.

This survey paper is organized as follows: Section 2 outlines the physical characteristics of muons, Section 3 examines the principles of muon navigation, Section 4 discusses the advancement of present studies, and Section 5 provides the challenges of muon navigation. Section 6 concludes this study.

2. Muon Physical Properties

Cosmic ray muons are second-generation leptons with a mass of 105.7 MeV/c^2, which is 207 times greater than that of an electron and 1/9 the mass of a proton. Muons possess an electric charge that can be either positive ($\mu+$) or negative ($\mu-$) and have a spin value of 1/2. Muons are a type of particle that is not stable and has an average lifetime of 2.2 μs. The decay of muons typically results in the formation of a minimum of three particles, including an electron with the same charge as the muon, as well as two different types of neutrinos.

Muons have a significantly greater mass than electrons, and because of this, they experience considerably less radiation loss than electrons. The primary mechanisms responsible for the energy loss of muons with energies in the range of several GeV as they traverse a material are atomic ionization and Coulomb scattering with atomic nuclei. Atomic ionization involves muons interacting with electrons in the material, leading to the ionization of atoms. At the same time, Coulomb scattering refers to the deflection of muons by the electric fields of atomic nuclei. Understanding these processes is crucial for muon tomography. As a result, they retain a significant amount of energy during their journey and possess greater penetrating power compared to X-rays and other forms of radiation. Cosmic ray muons are generated in the atmosphere at an altitude of 10–20 km and travel at a velocity near that of light. According to the theory of relativistic time dilation, the observable lifetime of a muon on the ground is significantly greater than the 2.2 μs in its stationary reference frame. Consequently, muons remain detectable in the Jinping Mountain underground laboratory in Sichuan, which has a rock thickness of around 2700 m [36]. This is striking proof of the accuracy of special relativity.

2.1. Observed Muon Flux

At altitudes of 5–6 km, the flux of muons is comparable to or exceeds that of protons. At an altitude of around 2 km, the quantity of muons is roughly tenfold more than that of protons. At sea level, the number of protons is 100 times less than that of muons, and muons with a momentum larger than 1 GeV/c are measured at 60–70 $m^{-2}s^{-1}sr^{-1}$. On average, around 10,000 muons hit a square meter of the ocean surface per minute, corresponding to a frequency of 170 Hz per square meter. Approximately 600 muons pass through the human body each minute, whereas the hand encounters 1 muon each second [37]. The observations may deviate from the above data due to several factors such as the station altitude, solar activity, the magnetic fields of the Earth and Sun, and weather conditions [38].

Physicists have conducted extensive muon flux measurements in various corners of the Earth. These experiments in the atmosphere, on the ground, in subterranean tunnels and caves, underwater, and other locations provide extensive fundamental data for the study of muon characteristics. Enqvist et al. [39] used the same detector to measure the fluxes at different depths in the Pyhäsalmi mine in central Finland. Bergamasco et al. [40] have been making measurements at a specific site in the Mont Blanc Tunnel, which varies in depth from 50 m west to 4330 m. During 645.2 days of observation, Guo et al. [41] discovered 264 high-energy muons at the 2700 m Jinping Mountain underground laboratory. Table 1 also summarizes several other observed results, where the second column is the subsurface depth of soil or rock, and the third column indicates the equivalent depth at which the density is converted to water.

Table 1. Flux of muons at different depths underground.

Location	Depth		Intensity ($\mathrm{m^{-2}s^{-1}}$)
	(m)	(w.e.) (m)	
Pyhäsalmi, Finland [39]	0	0	180 ± 20
Mont Blanc, France [40]	41	106	5.82 ± 0.05
Holborn, UK [42]	72	183	2.03 ± 0.07
Homestake, USA [43]	240	712	$(6.6 \pm 0.2) \times 10^{-2}$
Pyhäsalmi, Finland [39]	400	980	$(2.1 \pm 0.2) \times 10^{-2}$
WIPP, USA [44]	655	1585	$(4.8 \pm 0.1) \times 10^{-3}$
Soudan, USA [45]	713	1950	$(2.0 \pm 0.2) \times 10^{-3}$
Boulby, UK [46]	1070	2805	$(4.1 \pm 0.2) \times 10^{-4}$
Gran Sasso, Italy [47]	1462	3800	$(3.4 \pm 0.01) \times 10^{-4}$
SURF, USA [48]	1478	4227	$(4.6 \pm 0.33) \times 10^{-5}$
Sudbury, Canada [49]	2196	6150	$(3.8 \pm 0.4) \times 10^{-6}$
Jinpingshan, China [41]	2700	7560	$(3.5 \pm 0.2) \times 10^{-6}$

The table indicates that muons have a great penetrating ability to reach several kilometers underground, which is very important for realizing global ubiquitous positioning. However, most muons cannot reach the extensive depths of seawater, because numerous data show that the average energy of muons on the Earth's surface is only 3–4 GeV. These detected muons of several thousand meters represent a limited quantity of high-energy muons observed over a long time. In practice, the flux at a given depth underwater is typically modeled using the depth vertical intensity relation function as

$$I(h) = A \cdot (\frac{h_0}{h})^{\alpha} \cdot e^{-\frac{h}{h_0}} \tag{1}$$

where I is the intensity and h is the depth. A, h_0, and α are fit from the measured data [50]. However, these simulated parameters of vertical equivalent underground intensity are only approximately at zenith angles below 30° [51]. In addition, various datasets are usually combined but not corrected and compensated for, so the fit may only pursue experiments with small errors.

From Equation (1), we can find that muon penetration is influenced not only by energy but also by the incident angle. Let I_0 represent the entire muon flux, and the flux at incident angle θ can be expressed as

$$I(\theta) = I_0 \cos^{\alpha} \theta \tag{2}$$

where α is the angular dependence parameter, which characterizes the rate at which the muon flux decreases with an increasing incident angle. The parameter α varies slightly with the change in location of the measurements, the altitude, and the muon energy intervals. In general, it can be assumed that $\alpha = 2$, i.e., the flux of muons is proportional to $\cos^2 \theta$ [52].

It can be seen that the muon flux is not only related to the depth of the subsurface but also to the azimuth angle. Thus, the count of muons can be expressed as a function of energy and the azimuth angle. There are two methods to describe it. One is a full Monte Carlo simulation of the opening of atmospheric clusters produced by primary cosmic radiation, taking into account geomagnetic- and altitude-dependent muon interactions. An example is CORSIKA [53]. The other is a parametric model based on the fitting of experimental values, such as the Gaisser Model [54], Gaisser/Tang Model [55], Bugaev/Reyna Model [56], etc. Other algorithms such as the EcoMug Model [57] are sometimes used [58].

The Gaisser Model was proposed in 1990 and is concerned with the production of muons from the two-body decay of pions and kaons. When the muon energy $E \gg \epsilon_\mu$ (where $\epsilon_\mu = 1.0$ GeV is the critical energy of atmospheric muons), muon decay and energy loss in the atmosphere can be neglected. This is the cosmic ray muon flux (in GeV) at sea level given by Gaisser:

$$\frac{\mathrm{d}I}{\mathrm{d}E} = 0.14\left(\frac{E}{\mathrm{GeV}}\right)^{-2.7}\left(\frac{1}{1+\frac{1.1E\cos\theta}{115\ \mathrm{GeV}}} + \frac{0.054}{1+\frac{1.1E\cos\theta}{850\ \mathrm{GeV}}}\right) \tag{3}$$

Although the muon flux expressed in the above equation is relatively stable, it is still affected by several different factors in space and time [59]:

(1) Altitude: The muon flux increases with altitude from sea level upward, primarily because the number of low-energy muons lost through interactions with the atmosphere decreases as elevation rises.

(2) Latitude: The flux is lower near the equator due to shielding from the Earth's magnetic field.

(3) Solar activity: The intensity of the low-energy part of the muon energy spectrum depends on the solar magnetic deflection and is inversely correlated with solar activity.

(4) Atmospheric pressure (short time effect): Higher pressure in the lower atmosphere decreases the flux because the increased volume of air absorbs the lower energy muons.

(5) Upper atmospheric temperature (seasonal effect): The temperature of the upper atmosphere increases during the summer months, increasing the mean free path of pions and kaons, and thus the likelihood that they will decay into muons.

2.2. Energy-Loss Models

The energy value of a muon directly affects its penetrating capability. Energy loss can be classified into two types: continuous and random. The former relates to the electromagnetic interaction between the charged muon and the atoms in the material, resulting in the ionization of the atoms. The muon continuously loses energy as its flight distance increases. In the latter case, the initial energy is relatively large, and the remaining stochastic process is just as significant as the energy loss from the ionization effect. The density and thickness of the medium solely influence the rate of energy loss, meaning the muon's density in material and the distance of flight serve as the primary theoretical foundation for muon detection [60].

The Bethe–Bloch equation, first published in 1930 [61], and its improved version [62], expresses the mass loss power (in $\mathrm{MeVg^{-1}cm^2}$) as

$$\left\langle -\frac{\mathrm{d}E}{\mathrm{d}X}\right\rangle = Kz^2\frac{Z}{A}\frac{1}{\beta^2}\left[\frac{1}{2}\ln\frac{2m_ec^2\beta^2\gamma^2W_{max}}{I^2} - \beta^2 - \frac{\delta(\beta\gamma)}{2}\right] \tag{4}$$

where $X = x{\cdot}\rho$ is called opacity and ρ is the density of crossed materials in $\mathrm{g/cm^3}$, K is a proportionality coefficient, the value is 0.3071 $\mathrm{MeVg^{-1}cm^2}$, z is the charge of the incident particle ($z = 1$ for muon), Z and A are the atomic number and mass of the absorber, I is the average excitation energy, the approximation is expressed as $I = 16Z^{0.9}$ eV ($Z > 1$), m_e is the electron mass, W_{max} is the maximum energy transfer in a single collision, β is the relativistic velocity, γ is the Lorentz factor, $\beta\gamma = p/Mc$ (p is momentum, M is mass, and c is the speed of light), $\delta(\beta\gamma)$ is the density of the loss of energy from ionization effect correction. For high-energy particles, $-\delta(\beta\gamma)$ approximation is $2\ln\gamma + \zeta$, where ζ is a constant term dependent on matter. At non-relativistic energies, $\left\langle -\frac{\mathrm{d}E}{\mathrm{d}X}\right\rangle$ as a whole is affected by the β^{-2} factor and decreases with increasing velocity v until it is minimized at $v = 0.96c$. In practice, most relativistic particles, such as cosmic ray muons, have an average energy-loss rate close to the minimum.

Equation (4) describes the mass loss power for a given simple material. A mixed material can be found by integrating as follows:

$$\frac{1}{\rho}\frac{\mathrm{d}E}{\mathrm{d}X} = \sum_i \frac{w_i}{\rho_i}\left(\frac{\mathrm{d}E}{\mathrm{d}x}\right)_i \tag{5}$$

where w_i is the weight of the ith material in the mixture.

In practice, it is important to know how far the muon can penetrate the matter before it loses its energy, which depends on the type of material and the energy of the muon. For simplicity, Equation (4) is sometimes written as

$$\left\langle -\frac{\mathrm{d}E}{\mathrm{d}X}\right\rangle = a(E) + b(E)E \tag{6}$$

where the parameters a and b depend on the muon energy and on the atomic composition of materials through the average of the ratios Z/A and Z^2/A. Groom et al. [63] give relevant parameters for various materials.

Since muons decay because they interact with the matter, their energy loss is proportional to the length and density of the crossed materials. If it is assumed that the muon passes through matter in a straight line; the relationship between the opacity X and the density ρ of the penetrating materials and the path length L can be expressed as

$$X(L) = \int_L^\infty \rho(x)\mathrm{d}x \tag{7}$$

If the density is constant along L, the equation becomes

$$X(L) = \rho L \tag{8}$$

Otherwise, the average density $\overline{\rho}$ can be used to represent

$$X(L) = \overline{\rho} L \tag{9}$$

3. Muon Measurements

The device that measures information such as the number, momentum, direction, and time is called a muon detector. For multiple kinds of applications, a lot of muon detectors have been specifically conceived, developed, and manufactured. These detectors exhibit exceptional detection performance and are highly reliable. The detector is the basic observing equipment of the muon navigation, and its type and performance have a direct impact on positioning.

3.1. Detectors

Presently, widely used detectors include scintillator detectors, gas detectors, and nuclear emulsion detectors, alongside the recently devised ring image Cherenkov detector [37]. These detectors are suitable for different scenarios depending on the application requirements. Overall, it seems that the choice of a detector depends on several factors [64].

(a) Size: In order to enhance statistics and improve the ability to detect the direction of cosmic ray muons, big detectors are necessary. These detectors typically have dimensions ranging from 30 × 30 cm^2 to several m^2. The use of larger detectors helps to reduce observing time and minimize statistical errors.

(b) Resolution: The resolution is a crucial factor of measurement precision, which can be divided into angular resolution and location resolution. Various applications have distinct resolution requirements, often ranging from sub-milliradians to ten milliradians (mrad) in terms of angular resolution. The relationship between the angular resolution $\Delta\alpha$ and the location resolution Δr is given by the equation $\Delta r = L \times \Delta\alpha$, where L represents the distance between the detector and the observed item. The resolution of the detector's position is often constrained to $p/\sqrt{12}$, where p represents the pixel size [59]. This limitation is necessary to strike a compromise between the size of the detector and its angular resolution.

(c) Stability: The temperature, humidity, weather conditions, and power supply directly influence the detector's performance. Furthermore, the muon flux is typically low and requires prolonged observation.

The principle of a scintillator detector is to utilize the photons generated when a particle passes through a scintillator material (e.g., plastic or crystal), which are then converted into an electrical signal and processed by a photoconverter. Commonly used photoelectric converters include photomultipliers (PMTs), silicon photomultipliers (SiPMs), and so on. Scintillator detectors have high sensitivity, fast response times, and high energy resolution but are relatively costly and have certain requirements on the temperature and humidity of the environment.

Gas detectors use special gases such as argon, methane, etc., as a detection medium and make observations using the ionization that occurs with the gas when the muon passes through. Overall, the gas detectors have high sensitivity and spatial resolution with good scalability but require high gas purity.

The principle of a nuclear emulsion detector is similar to that of a conventional film camera. When a muon passes through, a light-sensitive material containing silver salts (e.g., silver bromide) interacts with the muon and leaves a latent image. By analyzing the latent image, the precise trajectory of the muon can be obtained, resulting in high spatial resolution and no need for a power source, which makes it suitable for long-term observations but not for real-time processing.

Cherenkov radiation is produced when charged particles travel faster than light in a medium. In order to collect the photons produced by Cherenkov radiation, a light collection system is usually required. Cherenkov detectors have high velocity resolution and do not require external energy input, making them suitable for long-term observations. Their performance is mainly limited by the light collection system.

3.2. Time of Flight

In order to measure the TOF of a muon between different detectors, a common approach is to integrate a time-to-digital converter (TDC) or an analog-to-digital converter (ADC) into the board design or chip-level integration. Since the muon velocities are generally close to the speed of light c, and the typical size of the detectors is on the meter scale, advanced TOF measurement techniques should achieve a sub-nanosecond time resolution.

In current high-energy physics, the fully developed and widely used TOF measuring technology is based on the plastic scintillation counter read out by the PMT. Figure 1 is a typical device.

In the final processing step, two pulse signals with a time interval of τ are digitized by the ADC and sent to the processor for further analysis. The digitized signals can be converted to frequency domain signals by means of the discrete Fourier transform (DFT). A cross-correlation operation is then performed to extract the frequency and phase information of its cross-correlation function. Accordingly, Wang achieved a time precision better than 50 ps [65]. Augusto, on the other hand, used the Hilbert transformation incorporated into LabVIEW 7.1 software to measure the time with a precision of 1.5 ns between two detectors separated by 3 m [66].

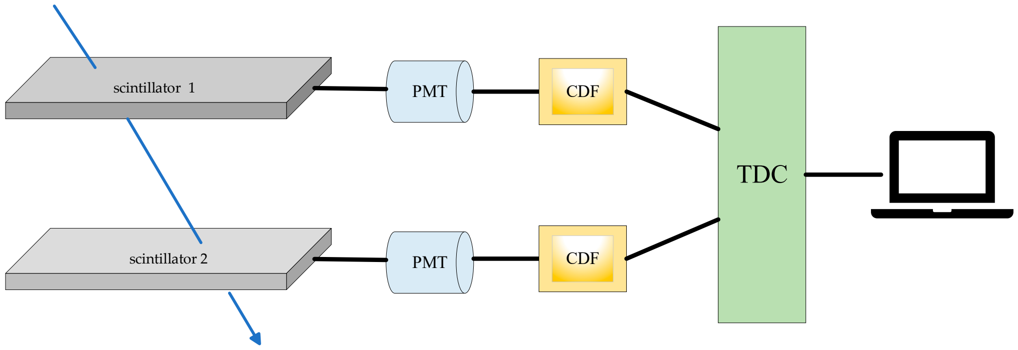

Figure 1. When a muon hits the upper detector, its interaction with a scintillator produces scintillation light. Amplified by the PMT, the time information is extracted by the constant fraction discriminator (CFD) and converted into an electrical signal by the TDC. The computer records the moment. Similarly, when the muon hits the lower detector, the computer records another moment, and the difference between these two moments is the TOF of the muon between the two detectors. The blue line is the direction of muon flight. When the two detectors are far apart, the TDC modules can be designed independently.

The amount of scintillator light, rise time, thickness, attenuation length, and the effective light-receiving area of the PMT primarily determine the temporal resolution of scintillator detectors. Niwase et al. [67] describe an alpha-TOF detector with an ionization chamber, electron multiplier, and signal output. In addition, Chaber et al. [68] mention the use of TOF in particle physics experiments, such as detector designs in the ALICE and ATLAS experiments, using a fine-particle gas chamber (MRPC) to achieve high temporal resolution. Sykora et al. [69] describe the performance of the ATLAS ToF detector in proton detection, involving time measurement and signal processing.

3.3. Incident Coordinates

High-energy physics experiments sometimes necessitate the tracking of muons by measuring parameters such as time, velocity, momentum, and coordinates. The data for the muon navigation system are established by determining the incident coordinates of the muon at a reference detector. By measuring the exact position of the muon at each layer as it traverses a multi-layer detector, the angle of incidence may be computed. This enables AOA localization. This information is crucial for determining the object's position in subsurface environments.

The principle of incident coordinate measuring differs depending on the type of detector employed. Each is delineated below by detector types.

3.3.1. Gaseous Detectors

Gaseous detectors, including drift tubes, multi-wire proportional chambers (MWPCs), and drift chambers (Figure 2) [70], dominate muon tracking due to their high spatial resolution and adaptability.

They can utilize various inert gases such as argon, xenon, and hydrocarbons as working gases for proportional detector operation. Muons will ionize gas atoms when passing through the detector. If an external electric field is applied, a Townsend avalanche will occur near the metal wire. The simplest construction method is a row of aluminum tubes stacked side by side. In practical applications, a large number of drift tubes are used to form the detection plane.

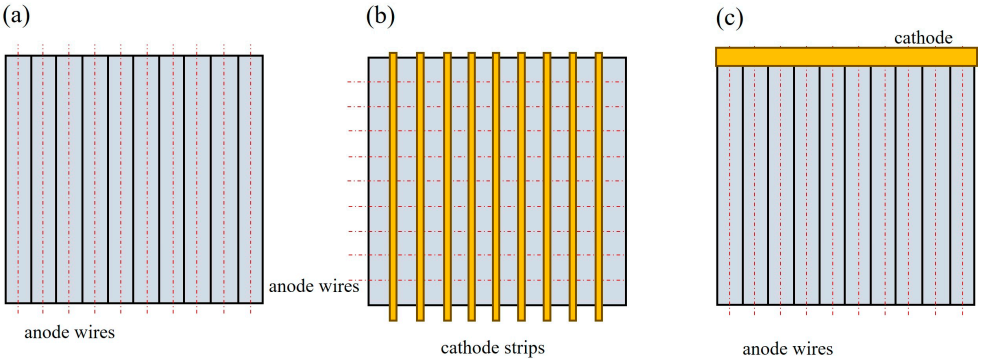

Figure 2. The schematic of the gas detector structure: (**a**) drift tube; (**b**) multi-wire proportional chamber; (**c**) drift chamber. The dashed line is anode wire. In the center of each drift tube is an anode wire used to collect electrons generated by ionization of muons and the gas. The MWPC consists of multiple cathode strips separating the anode wires to get more precise location. The drift chamber calculates the distance between the muon and anode wires by measuring the time it takes for the electrons to travel through the gas.

The MWPC has been the most popular choice for high-energy physical track detection systems, especially in research that needs very high space resolution. The MWPC [71] is a planar detector composed of multiple proportional counters. Nevertheless, the MWPC is limited to providing coordinates that are perpendicular to the wire rather than parallel to it. It is necessary to use cathode strips in order to achieve a spatial resolution of 50 µm along the wire direction. Using an anode of numerous strips of insulating or semiconductor materials instead of filaments can significantly boost the count rate of a microstructural gas detector, such as MWPC [72,73]. This increase is more than 10 times greater, resulting in a count rate that is one order of magnitude higher. As a result, this type of gas detector is currently the most commonly employed.

The drift chamber determines the distance traveled by particles passing through the chamber by measuring the time delay between the charge hitting the anode wire and the particles reaching the chamber. Reducing either the number of wires or the spacing between them can greatly enhance the space resolution [74]. When the drift velocity is v and the electronic time resolution is t, the space resolution should be vt. Notice that this does not account for electron diffusion. A large drift chamber typically has a spatial resolution of 200 µm, whereas a small drift chamber has a space resolution of 20 µm. Table 2 lists the gas detectors developed by the main relevant institutions.

Table 2. Gas detectors developed by major institutions.

Detector Type	Researcher	Layers	Resolution (mm)	Size (cm^2)
Drift tube	LANL [75]	6	0.4	120 × 120
	LANL [76]	12	2 mrad	365 × 365
	INFN [77]	8	—	200 × 200
	CIAE [78]	6	0.5	120 × 240
MWPC	UTokyo [79]	6	1.8	20 × 32
Rift chamber	INFN [80]	8	0.2	300 × 250
	CRIPT [81]	6	1.7	240 × 120
	RIHEP [82]	8	0.2	300 × 300
	AWE [83]	12	1.2	180 × 60

3.3.2. Scintillation Detectors

The structure diagram of the plastic scintillator detector includes a stacked layout structure [84], triangular interlocking structures [85], a scintillating fiber tiling structure [86], a lateral coupling structure [87], and a compact structure [88].

Istituto Nazionale di Fisica Nucleare (INFN) designed a lightweight muon transmission imaging detector in the Muon Imaging for Miningand Archaeology (MIMA) project using a stacked scintillator layout (Figure 3a) to measure the muon vertical flux [84]. The most commonly used is the staggered arrangement of triangular scintillator strips (Figure 3b), such as the MU-RAY [89], MURAVES [85], the muon imaging system designed by the Canadian CRIPT cooperation [90], and the small cosmic ray muon imaging prototype of Lanzhou University—LUMIS (Lanzhou University Muon Imaging System) [91]. In addition, scintillation fibers can also be used for the construction of muon imaging detectors, as shown in Figure 3c. In 2022, Zhai et al. proposed a lateral coupling arrangement of plastic scintillator strips [87] (Figure 3d). Figure 3e is mainly a drilled muon detector used in special application scenarios [88].

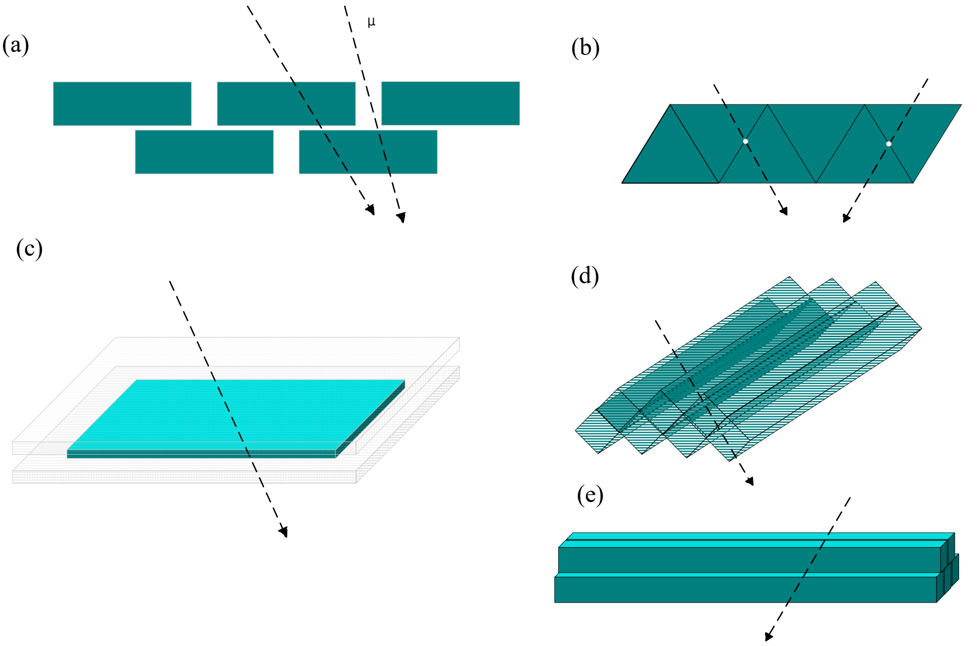

Figure 3. The structure diagram of the plastic scintillator detector: (**a**) stacked layout structure; (**b**) triangular interlocking structure; (**c**) scintillating fiber tiling structure; (**d**) lateral coupling structure; (**e**) compact structure. The dashed lines are the incident directions of muons.

Regardless of the geometric configuration, the detection principle involves scintillation photons emitted along the particle trajectory being collected either via light guides, through wavelength-shifting fibers (WLSs) typically encapsulated within the scintillator bar itself, or by direct coupling to SiPMs (or PMTs) attached to the scintillator bar. The electrical signals are then transmitted to a computer, where algorithmic processing determines the position.

Obviously, the position resolution of a scintillator detector is directly related to the size of the scintillator strips. Usually, when a muon hits any position of the strip, a light signal is generated, and different light signals will not be generated due to different hit positions. Therefore, the position accuracy is the size of a single scintillator strip. The smaller the strip, the higher the coordinate measurement accuracy.

3.3.3. Other Detectors

Strips replace the anode in the microstrip gas chamber (MSGC), a downsized multifilament proportional chamber. Muon imaging has a spatial resolution of 20–30 µm, although it is subject to an aging effect [92]. Currently, micromegas [93] and gas electron multiplier [94] are the most widely used detectors, which exhibit a gain of at least two orders of magnitude higher than microstructural gas detectors.

Silicon microstrip detectors can achieve a spatial resolution of approximately 10 µm or higher [95]. They can be used as vertex detectors in the central region of particle physics experiments or as focal plane detectors on satellites. Although semiconductor position-sensitive detectors exhibit superior spatial resolution, their unit area cost is significantly higher compared to the aforementioned detector technologies.

Another detector is the Cherenkov detector. The physical principle of this method, as stated in Section 3.1, involves the emission of electromagnetic radiation when charged particles traverse a medium (such as air) at speeds exceeding the phase velocity of light in that medium. The Cherenkov light generated along the muon path is imaged as a characteristic ring-shaped pattern (easily distinguishable from most background particles), where both the shape and brightness allow for the reconstruction of the muon's trajectory and energy [70]. Cherenkov techniques are widely used in astroparticle experiments. At the same time, the technology is expected to be used for underground or underwater muon navigation. Table 3 lists some past, present, and future international, large Cherenkov detector projects.

Table 3. Past, present, and future international, large Cherenkov detector projects.

Project	Location	Cherenkov Medium	Size (km^3)
DUMAND [96]	Hawaii	natural water	-
NT200 [97]	Lake Baikal	natural water	10^{-4}
AMANDA [96]	South pole	natural ice	0.015
IceCube [98]	South pole	natural ice	1.0
Baikal-GVD [99]	Lake Baikal	natural water	>0.5
KM3NeT [100]	Mediterr. Sea	natural water	1.2
Super-K [101]	AbandonedArsenic mine	ultrapure water	5×10^{-5}
IceCube Gen 2 [102]	South pole	natural ice	8
TRIDENT [103]	South China Sea	natural water	7.5

4. Muon Navigation

Navigation refers to the system or process that guides the direction, path, or information positioning in different fields. The core function is to help users achieve the arrival of the target location or the accurate acquisition of information. Muon navigation uses muons to replace the electromagnetic wave signal of traditional GNSS, uses reference detectors with known positions, and obtains the position of the positioning detector through mapping methods such as resection.

The trajectory of the muon is nearly straight in some low-density materials due to the small-angle Coulomb scattering. Referring to the concept of tomography [104], the TOF and AOA between the two detectors can be measured by placing one detector high and the other low. The higher detector located on the exposed terrestrial surfaces, including the ground, building's roof, and ocean surfaces, is referred to as the reference detector, and its position can be determined by astrometry, GNSS, ground-based radio, or other technologies. The lower detector is the positioning detector fixed on the target to be deployed underground or underwater. It measures the time difference when muons pass through the reference detector and the positioning detector. The speed of muons in water is very close to the speed of light due to their high energy. At a depth of 500 m underwater, the speed of muon exceeds 0.9999999*c*. Consequently, the distance between the reference detector and the positioning detector can be determined, and thus, the unknown coordinates can be calculated by the principle of trilateral resection or angular resection.

4.1. Positioning Principle

In low-density materials, where Coulomb scattering is minimal, the muon trajectory deviates negligibly and can thus be modeled as a straight line. The distance between the detectors can be found by measuring the time difference between the passage of the muon through the two detectors. The muometric positioning system (μPS) [27] operates on a similar concept to GNSS, as depicted in Figure 4. R_1, R_2, and R_3 are the three reference detectors where their locations are known. The location of the positioning detector P is unknown. Because of the significant incidence of cosmic rays, the locator can be deployed in various environments, including outdoor, indoor, underwater, and underground. To enable both devices to detect the same muon, it is crucial that the positioning detector be located under the reference detectors.

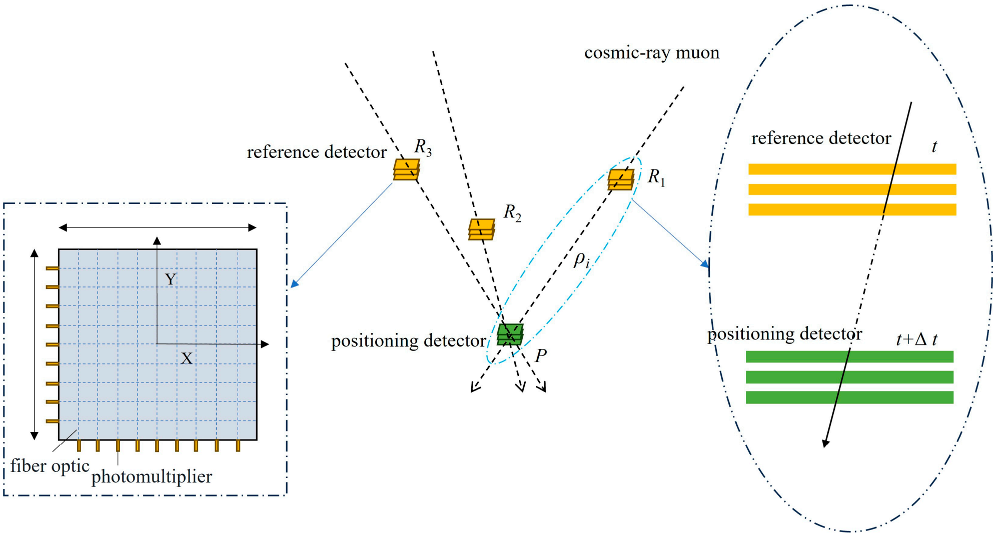

Figure 4. Trilateral resection of muon positioning. The distances are calculated by measuring the TOF of muons pass through the reference detectors and positioning detector alone the dashed line. It requires at least three muons to complete the observations.

The equation based on the spatial relationship between reference detectors and the positioning detector can be expressed as

$$\rho_i^2 = (X_i - X)^2 + (Y_i - Y)^2 + (Z_i - Z)^2 \tag{10}$$

where ρ_i is the distance between the ith ($i = 1, 2, 3 \cdots$) reference detector and the positioning detector, (X_i, Y_i, Z_i) are the known coordinates of the reference detector, and (X, Y, Z) are the unknown coordinates of the positioning detector.

Equation (10) contains three unknown variables. Therefore, it needs three distance observation functions to solve for an accurate coordinate. The value of ρ_i is determined by measuring the time difference between a muon passing through the reference detector and the detector being located, denoted as t_r, and the propagation velocity v (typically the speed of light c). Thus, it is crucial to ensure precise time synchronization between each reference detector and the positioning detector. Failure to do so will result in measurement errors. Undoubtedly, achieving time synchronization between reference detectors is very straightforward; however, synchronizing between the reference detectors and the positioning detector is a challenge. Define τ as the difference in system time between the synchronized reference detectors and the positioning detector. Equation (10) can be expressed as

$$(c \cdot t_i)^2 = (X_i - X)^2 + (Y_i - Y)^2 + (Z_i - Z)^2 + (c \cdot \tau)^2 \tag{11}$$

This equation has four unknown variables, and at least four reference detectors are required. Due to the random nature of muons, it is quite unlikely for four muons from the same time period to pass through various reference detectors and a positioning detector simultaneously. Consequently, the detector's clock stability is very important. As the depth increases, the amount of muons suitable for navigation decreases, resulting in a longer observing time. If there is a significant discrepancy in the accuracy of the clock in the detector, the value of τ in Equation (11) no longer remains constant, which directly affects the positioning performance.

The accuracy of measurement t_i in Equation (11) is directly related to the time resolution of the detector. This, in turn, impacts the final positioning accuracy. Currently, the detector is capable of recording the hit time of muons throughout all detection surfaces. However, the commonly used scintillator detector is unable to provide the trajectory of a particular muon or perform calibration for a specific muon. Hence, in order to determine t_i, it is necessary to obtain the number of muons observed by a pair of detectors that occur simultaneously. In this case, the time series of muons are recorded in both the reference detector and the positioning detector. When the muon signals hit both detectors within the time window T_W, the recorded data can be deemed to be in agreement if they are correlated in time. The TOF, denoted as t_i, is determined by the time difference between the two detectors when the overlap with the time series of the reference detector reaches its maximum peak. Hence, the selection of T_W has a direct influence on the measurement precision, which relies on the time resolution of the detector. In terms of reference detectors, scintillator detectors are often used because they can accurately measure positions to centimeter level, which is good enough for most navigation applications.

Trilateral positioning based on the TOF requires highly accurate time information to determine the time difference when the muon passes through the reference detector and positioning detector. AOA-based angular positioning is relatively much simpler and does not require precise time synchronization, as long as the incidence angle of the muon as it passes through the two detectors can be measured to complete the localization. As shown in Figure 5a, the incident zenith angle of the muon on the reference detector is θ_i, the incident azimuth angle is α_i, and the coordinates of the hit point are (X_i, Y_i, Z_i); at this time, there is the following relationship between the coordinates of the unknown point (X, Y, Z) and these observations

$$\begin{aligned} \tan\theta_i &= \frac{\sqrt{(X_i - X)^2 + (Y_i - Y)^2}}{Z_i - Z} \\ \tan\alpha_i &= \frac{X_i - X}{Y_i - Y} \end{aligned} \tag{12}$$

There are three unknown parameters in Equation (12), but only two observation equations, so additional conditions must be attached. If the perpendicular distance d between the reference detector and positioning detector has been obtained by other methods (e.g., pressure measurements), then we have

$$d = Z_i - Z \tag{13}$$

Or, if the TOF is measured at the same time as the angle, Equation (12) can be solved with Equation (11) together. Of course, it is not easy to directly measure either the perpendicular distance or the TOF. Therefore, it needs redundant observations to calculate the unknown coordinate of the positioning detector in practice.

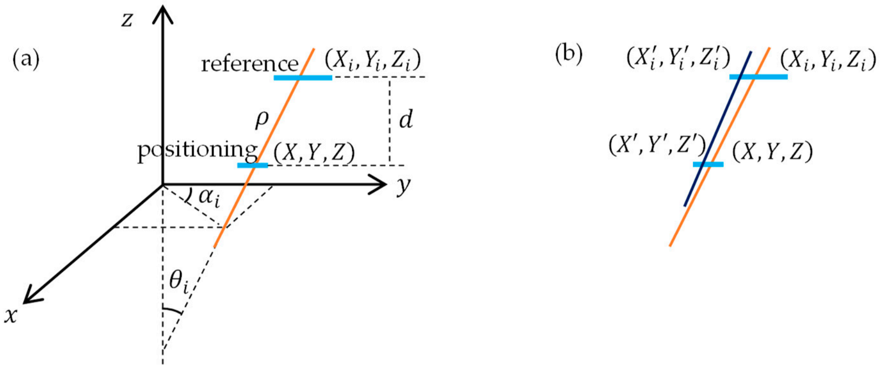

Figure 5. Angular resection of muon positioning. (**a**) A single muon passes through the reference detector and positioning detector; (**b**) two muons pass through the reference detector and positioning detector at different positions.

In Figure 5b, let there be another muon (dark blue trail) with an incident zenith angle of θ_i', an incident azimuth angle of α_i', and an incident point coordinate of $\left(X_i', Y_i', Z_i'\right)$ on the reference detector and (X', Y', Z') on the positioning detector, and then Equation (12) will have four observation equations. If the coordinate accuracy requirement is not particularly precise, when the size of the positioning detector is not too large, the coordinate of the hit point of the two muons can be considered to be the same.

$$\begin{aligned} X' &\approx X \\ Y' &\approx Y \\ Z' &\approx Z \end{aligned} \tag{14}$$

The unknown coordinates (X, Y, Z) can be solved using Equation (12). If the space resolution of the positioning detector is high enough, the coordinate difference $(\Delta X, \Delta Y, \Delta Z)$ between the two hits can be measured.

$$\begin{aligned} X' &= X + \Delta X \\ Y' &= Y + \Delta Y \\ Z' &= Z + \Delta Z \end{aligned} \tag{15}$$

It is also possible to solve the unknown coordinate. Therefore, the key factors for solving the unknown point coordinates are the angular resolution and space resolution of the detector.

4.2. Current Achievements

In 2020, Tanaka performed a proof-of-concept study on cosmic ray muon navigation within a laboratory environment [27]. He employed the Monte Carlo approach to simulate and evaluate the Coulomb scattering effect of relativistic muons on the seafloor. Subsequently, some lead blocks of different thicknesses were placed between the two detectors to simulate a propagation delay of 5 ms, corresponding to a distance of about 1.5 km. The experiments have demonstrated the theoretical feasibility of muon navigation, enabling three-dimensional positioning over distances of kilometers, supported by wired time synchronization. To eliminate the constraints of wired connections for time synchronization, Tanaka initiated indoor and subterranean physics demonstration tests for wireless muon navigation in 2022 [28] and established the inaugural wireless muometric navigation system (MuWNS) in 2023 [29]. They installed large reference detectors (total area of 4 m^2) on the sixth floor (above ground level) and receiver detectors with an area of 1 m^2 on the basement floor. Moreover, even with this configuration, it took 16 min to successfully track one point from the receiver [31]. The field testing of MuWNS was conducted at the Toranomon Hills Subway Station. He strategically placed four reference detectors on tall buildings near the metro station. Tanaka successfully achieved time synchronization between the reference stations by GPS. Each detector consisted of a square plastic scintillator with dimensions of 1×1 m^2 and a PMT element with a thickness of 2 cm. The moving station installed an oven-controlled crystal oscillator (OCXO) clock for timekeeping, synchronizing by GPS on the ground during initialization. The results of 1800 s observations show that the muon positioning precision is comparable to the GPS pseudorange single-point positioning results in Tokyo and even exceeds GPS performance in certain directions. In MuWNS, the principle is trilateral localization based on the TOF, which is determined by the time of muon traveling between the two detectors. The major reason for the positioning precision being limited to 2–14 m is the challenge of keeping time synchronization among all reference and positioning detectors. It presents difficulties for indoor navigation applications that necessitate more accuracy.

In order to achieve the ideal positioning accuracy at the centimeter level, Tanaka proposed the concept of vector muon navigation (MuWNS-V) based on incident angle measurements in 2023 [30] and derived the basic formula. Varga carried out experimental validation on this theory and predicted that the MuWNS-V could achieve sub-centimeter-level navigation, which can be applied to a variety of applications such as the operation of autonomous mobile robots in the future [32]. Two experiments were designed with 'LowRes' and 'HiRes' configurations (Figure 6). The 'LowRes' configuration used a smaller reference detector with an angular resolution of about 15 mrad, resulting in a positioning accuracy of 3.9 cm (RMS). The reference detector was 2.4 m above the positioning detector. The improved version utilized a larger size of reference detector and will be referred to as a 'HiRes' configuration. It also increased the angular resolution to approximately 6–8 mrad, using the same positioning detector. Furthermore, the detectors were located on two different floors of the building, with a height difference of 3.3 m, to enhance the positioning accuracy to better than 3 cm (RMS).

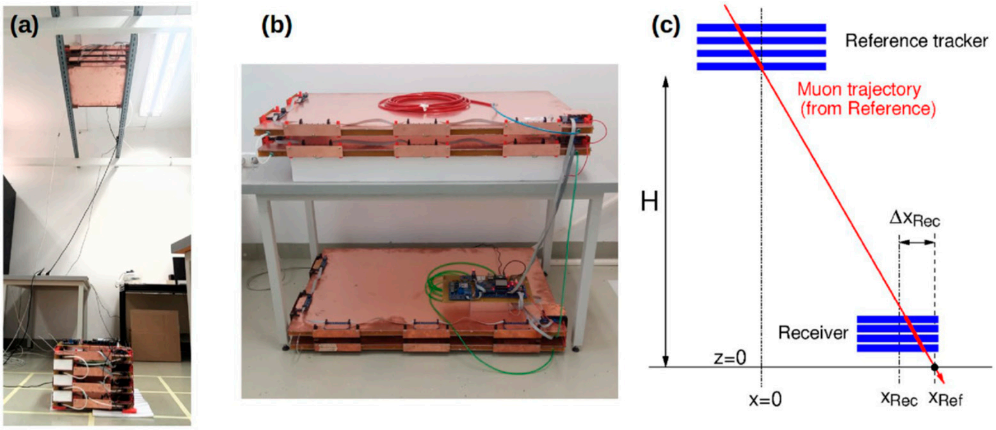

Figure 6. The experimental setup. (**a**) Photograph of the "LowRes" detector system, with a reference attached to the rails below the ceiling and the positioning on the ground. (**b**) Reference detector of the "HiRes" system. (**c**) Illustration showing the geometrical parameters [32].

Table 4 summarizes the results of the relevant experiments that have been carried out so far. It can be seen that the accuracy of TOF-based muon positioning is comparable to or even better than the accuracy of GNSS pseudorange single-point positioning in the urban canyon environments with a complex multipath, while the accuracy of AOA-based muon positioning is comparable to the accuracy of precision point positioning (PPP). Of course, the muon positioning accuracy is still only the laboratory accuracy, with less consideration of the errors in the observations, only at the level of positioning accuracy, and has been widely used with GNSS, so comparison is not comprehensive.

Table 4. Positioning algorithms and accuracy.

Technique	Algorithm	Measurement	Time Sync.	STD (m)	Max. (m)
MuWNS [29]	trilateral resection	TOF	yes	2.3 (H) 6.6 (V)	6.0 (H) 8.0 (V)
MuWNS-V [32]	angular resection	AOA	no	0.039 (H)	0.3 (H)
GNSS [105]	trilateral resection	pseudorange	no	16.3 (H) 16.7 (V)	66.6 (H) 46.2 (V)

Li et al. developed a comprehensive set of muon navigation theories [35], which they combined with the muon pseudorange measurement technique. Furthermore, they proposed the equivalent velocity calculation model and the muon sequence matching technique. The first model corrects the relativistic energy loss-induced flight pseudorange error, while the second technique addresses the random error in the pseudorange measurement. They also conducted some simulations to analyze the number of muon events that the detector can receive under various zenith angles, detector sizes, detector plate gaps, and muon flight distances. They demonstrated that the muon navigation update rate every 10 min can reach 5.989 in confined spaces at 100 m.

In September 2021, the U.S. Office of Naval Research (ONR) selected the muon placement approach for the second annual Global-X Challenge. The ONR also opted to co-fund this technique with the U.S. army development command. A multinational team of researchers from Japan, the United Kingdom, the United States, and Finland is working on a project to address the issue of GPS signals being unavailable in high latitudes by substituting muons for GPS satellite signals. The project will undergo additional testing in Finland's Arctic Lake region after its initial testing in the UK [106]. This testing will specifically involve subjecting the project to ice that is 1 m thick, as well as testing it in extreme temperatures of −20 °C and submerged conditions. After successfully conducting field experiments at the University of Sheffield, the research team intends to go to the underground environment of the University of Oulu, Finland. Subsequently, they performed the following tests at Kilpisjärvi Lake in northern Finland.

In the latest research results of Tanaka [107], an alternative concept of cosmic ray arrival time navigation is proposed to utilize the extended air shower time structure for higher rate localization. The 2D positioning accuracy is about 3–4 m (at 50 m apart).

5. Challenges

Tanaka has advanced from performing laboratory experiments to conducting underground field tests of muon navigation, which represents a notable progression. Nevertheless, there remain further domains to explore and study. The following outlines some challenges for the future development of muon navigation.

5.1. Navigation Signals

The flux of cosmic ray muons in the atmosphere varies with the zenith angle due to the differing free paths they travel. In the vertical direction, the flux is significantly higher than in the horizontal direction. At sea level, the muon flux is approximately 60–70 $\mathrm{m^{-2}s^{-1}sr^{-1}}$. However, the flux markedly decreases to 0.0004 $\mathrm{m^{-2}s^{-1}sr^{-1}}$ at a depth of 1000 m. To augment the muon flux, the most convenient and direct approach is to enlarge the detection area. Clearly, the most efficient and straightforward method is to expand the detection size. Expanding the sensing area will increase the submersible's energy consumption. Additionally, it will make the submersible larger, reducing its flexibility and making it difficult to fulfill the mission requirements. Consequently, the implementation mostly relies on the submersible's structure and the design of a detector of suitable dimensions.

Underwater positioning typically employs three approaches to meet its requirements. The first involves generating a high-energy particle source capable of penetrating an ideal thickness of water and receiving an ample quantity of high-energy muons at the desired depth. In 2022, the Defense Advanced Research Projects Agency (DARPA) launched the Muons for Science and Security Program (MuS2) with the goal of intentionally producing high-energy muons. Typically, high-energy muon production depends on the use of extensive scientific facilities, such as the Fermilab national particle accelerator in Illinois and the CERN accelerator in Switzerland. MuS2 proposes to utilize laser plasma acceleration (LPA) to generate 10 GeV particles within a few centimeters, as opposed to the hundreds of meters required by current state-of-the-art linear accelerators. The primary objective of MuS2 is to develop efficient and feasible methods for generating muons with energies greater than 100 GeV. Advancements in LPA, target design, and small laser driver technologies will achieve this [108].

Furthermore, employing alternative subatomic particles, such as neutrinos, instead of cosmic ray muons should be considered. A neutrino is a subatomic particle that lacks electric charge and travels at the speed of light. Stellar nuclear fusion, supernova explosions, or certain accelerators on Earth can generate it. Neutrinos possess remarkable penetration capabilities and precise directionality. NASA has introduced the 2015 Technology Roadmap, which highlights the development of neutrino-based communication, navigation, and tracking as a novel concept technology to be prioritized over the next two decades [109,110].

Additionally, it can integrate with other sensors to form a comprehensive multi-source integrated navigation system. Barriers or external interference in the surrounding environment often do not influence the IMU, thereby ensuring accurate navigation. However, even with a high-quality IMU designed for industrial use, the error in the estimating position will exceed 50 m within one minute due to gyroscope drift. Ring laser gyroscopes (RLGs), fiber optic gyroscopes (FOGs), and hemispherical resonant gyroscopes (HRGs) help us deal with the random walk error of angle and velocity, as well as the bias instability of gyroscopes and accelerometers. However, these alternatives come with drawbacks such as significant weight, high cost, and large power consumption. On the other hand, microelectromechanical system (MEMS) gyroscopes are lightweight and cost effective, but they have a deviation of $1000^\circ/\mathrm{h}$ [111]. To address the limitations of both methods, integrating the muon positioning system with the IMU proves to be a viable solution. The muon positioning system consistently corrects the IMU's short-term drift, and the IMU offsets its low update rate. Modern buildings commonly contain many Wi-Fi access points. Research has led to the implementation of fingerprint recognition, the TOF, AOA, and other methods for positioning. However, obstacles like metal or seawater, which block radio waves between the devices, can greatly diminish navigation quality or prevent access to the navigation signal altogether. The integration of the muon positioning system with the Wi-Fi indoor positioning system (IPS) will result in substantial advantages. Notable researchers have already created mobile phone apps, such as DECO and CRAYFIS, which use mobile phone camera sensors to identify cosmic rays [112]. By installing a reference detector on the ceiling of a local area and connecting it to mobile phones using a specific communication method, it is possible to calibrate the Wi-Fi positioning results every minute and provide absolute coordinates. This calibration takes into account the muon's sea level flux, which is approximately 1 $cm^{-2}s^{-1}sr^{-1}$.

5.2. Positioning Models

Physicists represented by Tanaka have carried out laboratory proof-of-concept and outfield tests for muon navigation and achieved better localization results. However, in these experiments, whether it is TOF-based trilateral localization or AOA-based angular localization, the localization models are still relatively simple, without taking into account the errors of various measurements, and without establishing comprehensive function models and random models.

Similarly to the GNSS, the muon navigation errors can be divided into three parts: signal source, detector, and propagation path. The signal source of muon navigation is natural cosmic ray muons, and its error mainly comes from the measurement error of the reference detector, including the accuracy of time, incident angle, and hit coordinate. Theoretically, the angular accuracy of a muon detector is usually a sub-milliradian to ten milliradians, i.e., between 20″ and 200″, which is not precise enough. However, the space resolution is relatively high, up to 50 µm, which is able to satisfy positioning needs. Even with inexpensive scintillator detectors, it is possible to reach the centimeter level, which is why Tanaka believes that the ideal accuracy for muon navigation is on the centimeter level. When using TOF-based muon navigation, regardless of whether it is a wired or wireless connection, time synchronization is the greatest challenge. In the case of a wired connection, the speed of signal transmission through the cable is significantly affected by the environment. If the distance between detectors is large, the time for cable signal transmission cannot be ignored. At this time, environmental changes such as temperature will impair the ability to synchronize. For a wireless connection, a highly precise master clock for the device is required. However, time drift will occur during long-term use. Tanaka hopes to solve this problem by using high-precision chip-scale atomic clocks [28]. In addition, in order to be able to receive more muons, it is usually necessary to use a larger area detector. In the propagation path, the Monte Carlo simulations proved that the muon can travel in a straight line in seawater. However, the real marine environment is very complex, especially with the existence of Coulomb scattering, although still seawater density does not change much; exactly how much impact there is on the muon propagation is unknown, but it also needs more extensive empirical verification. At the positioning terminal, the detector size cannot be as large as the reference detector due to carrier performance limitations, so the performance in time, angle, and coordinates is degraded. Further refinement of these error sources and analysis of the error magnitude to improve detector performance are important challenges to be addressed at this time.

In vector muon navigation, where the angles (including azimuth and zenith of incidents) are the main observations, the dependence on time synchronization is reduced, but there are still many drawbacks, especially in the consideration of practical applications. As can be seen from Figure 6, the experiment was conducted in the laboratory and did not take into account the motion pose of the carrier of the detector. Taking the marine application as an example, the reference detector at the sea surface is influenced by wind, waves, currents, etc., and the detector cannot be in a stationary state, so the measured angles must contain the pose information of the detector. Of course, these poses can be measured by GNSS to some extent. However, it is more difficult to obtain high-precision attitude information for submarine vehicles that are underwater.

5.3. Application Scenarios

Experiments conducted by Tanaka have demonstrated that muon navigation technology can offer a level of accuracy in positioning that is comparable to GNSS. This technology has the potential to deliver highly precise location services for underwater activities. However, the submerged current detector for this test only reaches a depth of 5 m, severely restricting potential applications due to the limited deployment of the reference detector. Furthermore, the lack of detectable muons makes it impossible to meet the requirements for real-time navigation in the deep-water region of the ocean. Nevertheless, it can be integrated with additional sensors to enhance localization efficacy by prolonging the observation duration. When integrated with INS in a submersible, the muon navigation offers periodic calibrations to mitigate the drift error of the INS and facilitate rapid calibration. Furthermore, the creation of a subsurface geodetic datum network can leverage long-term observations to amass a substantial quantity of muons for achieving high-precision positioning.

While muons may have limited applicability in marine environments, they can be highly valuable in indoor and underground settings where people reside for extended periods of time. Indoors and underground positioning mostly depends on imprecise and varied local positioning methods, such as INS, geomagnetism, UWB, Wi-Fi, vision, and Lidar. However, achieving consistency between indoors and outdoors is challenging. Extending the high-precision Earth reference frame, established through space geodetic technologies, to indoor and underground environments is challenging. On the other hand, muon navigation enables GNSS high-precision positioning of the reference detector. This enables consistent navigation both indoors and underground by transmitting the reference datum to the positioning detector. A cosmic ray muon navigation system (CRoNS) [113] is being proposed for navigation purposes in urban subterranean environments and for the creation of a spatial datum that integrates both above- and belowground. They expect approximately 156 such muon showers per second, with the number from 1000 TeV protons being considerably fewer (around 0.1) but with a muon count exceeding 10,000. This is merely a basic concept, and substantial subsequent efforts are required to actualize it.

6. Conclusions

Cosmic ray muons, prevalent in the Earth's atmosphere, are more resistant to jamming and spoofing than radio signals. They can penetrate both underground and underwater, making them a suitable and dependable positioning signal in GNSS-denied scenarios. At the beginning of this paper, the physical properties of muons are explained. Then, the principles of muon positioning and the methods for measuring related quantities are elucidated. Finally, the results of the studies on muon positioning are consolidated, and the challenges are discussed.

The limited availability of naturally detectable muons and dependence on high-precision timing instruments restricts current muon positioning. As a result, muon positioning technology is not yet widely adopted; yet, it possesses potential for underwater and underground navigation. A comprehensive analysis of muon positioning, in conjunction with additional signals like INS, can provide frequent calibration for underwater vehicles in deep water and reduce INS error drift. Muon positioning possesses considerable potential applications in geodesy, facilitating the establishment of geodetic datums in GNSS-denied environments. We can expand the current geodetic spatial datum (e.g., international terrestrial reference frame (ITRF)), which is presently restricted to outdoor surfaces, to include interior, subterranean, and underwater environments through extended continuous static observation, thus achieving the unification of high-precision geodetic datum across the entire geographic domain.

Author Contributions: Conceptualization, D.Z. and L.L.; investigation, P.L.; writing—original draft preparation, D.Z. and P.L.; writing—review and editing, L.L. All authors have read and agreed to the published version of the manuscript.

Funding: This research was funded by the National Natural Science Foundation of China, grand number 42474043, Key Laboratory of Smart Earth, grand number KF2023YB01-05 and Natural Science Foundation for Excellent Young Scholars of Henan Province, grand number 252300421205.

Conflicts of Interest: The authors declare no conflicts of interest.

References

1. Sakpere, W.; Adeyeye-Oshin, M.; Mlitwa, N. A state-of-the-art survey of indoor positioning and navigation systems and technologies. *S. Afr. Comput. J.* **2017**, *29*, 145–197. [CrossRef]
2. Aparicio, J.; Álvarez, F.J.; Hernández, Á.; Holm, S. A survey on acoustic positioning systems for location-based services. *IEEE Trans. Instrum. Meas.* **2022**, *71*, 8505336. [CrossRef]
3. Tiemann, J.; Schweikowski, F.; Wietfeld, C. Design of an UWB indoor-positioning system for UAV navigation in GNSS-denied environments. In Proceedings of the 2015 International Conference on Indoor Positioning and Indoor Navigation (IPIN), Banff, AB, Canada, 13–16 October 2015; IEEE: Piscataway, NJ, USA, 2015; pp. 1–7. [CrossRef]
4. Zhang, H.; Ye, C. A visual positioning system for indoor blind navigation. In Proceedings of the 2020 IEEE International Conference on Robotics and Automation (ICRA), Paris, France, 31 May–31 August 2020; IEEE: Piscataway, NJ, USA, 2020; pp. 9079–9085. [CrossRef]
5. Ruan, Y.; Chen, L.; Zhou, X.; Liu, Z.; Liu, X.; Guo, G.; Chen, R. iPos-5G: Indoor positioning via commercial 5G NR CSI. *IEEE Internet Things J.* **2022**, *10*, 8718–8733. [CrossRef]
6. Zhao, H.; Zhang, N.; Xu, L.; Lin, P.; Liu, Y.; Li, X. Summary of research on geomagnetic navigation technology. *IOP Conf. Ser. Earth Environ. Sci.* **2021**, *769*, 032031. [CrossRef]
7. Javed, W.; Ghani, S.; Elmqvist, N. Gravnav: Using a gravity model for multi-scale navigation. In Proceedings of the International Working Conference on Advanced Visual Interfaces, Naples, Italy, 22–25 May 2012; pp. 217–224. [CrossRef]
8. Yang, Y.; Xu, T.; Xue, S. Progresses and Prospects in Developing Marine Geodetic Datum and Marine Navigation of China. *Acta Geod. Cartogr. Sin.* **2017**, *46*, 1–8. [CrossRef]
9. Boguspayev, N.; Akhmedov, D.; Raskaliyev, A.; Kim, A.; Sukhenko, A. A comprehensive review of GNSS/INS integration techniques for land and air vehicle applications. *Appl. Sci.* **2023**, *13*, 4819. [CrossRef]
10. Kim, Y.; Hwang, D.H. Vision/INS integrated navigation system for poor vision navigation environments. *Sensors* **2016**, *16*, 1672. [CrossRef]
11. Liu, P.; Wang, B.; Deng, Z.; Fu, M. INS/DVL/PS tightly coupled underwater navigation method with limited DVL measurements. *IEEE Sens. J.* **2018**, *18*, 2994–3002. [CrossRef]
12. Yang, C.; Cheng, Z.; Jia, X.; Zhang, L.; Li, L.; Zhao, D. A novel deep learning approach to 5g csi/geomagnetism/vio fused indoor localization. *Sensors* **2023**, *23*, 1311. [CrossRef]
13. Yang, Y. Concepts of comprehensive PNT and related key technologies. *Acta Geod. Cartogr. Sin.* **2016**, *45*, 505–510. [CrossRef]
14. Marteau, J.; Gibert, D.; Lesparre, N.; Nicollin, F.; Noli, P.; Giacoppo, F. Muons tomography applied to geosciences and volcanology. *Nucl. Instrum. Methods Phys. Res. Sect. A Accel. Spectrometers Detect. Assoc. Equip.* **2012**, *695*, 23–28. [CrossRef]
15. Del Santo, M.; Catalano, O.; Cusumano, G.; La Parola, V.; La Rosa, G.; Maccarone, M.C.; Mineo, T.; Sottile, G.; Carbone, D.; Zuccarello, L.; et al. Looking inside volcanoes with the imaging atmospheric Cherenkov telescopes. *Nucl. Instrum. Methods Phys. Res. Sect. A Accel. Spectrometers Detect. Assoc. Equip.* **2017**, *876*, 111–114. [CrossRef]
16. D'Alessandro, R.; Ambrosino, F.; Baccani, G.; Bonechi, L.; Bongi, M.; Caputo, A.; Ciaranfi, R.; Cimmino, L.; Ciulli, V.; D'Errico, M.; et al. Volcanoes in Italy and the role of muon radiography. *Philos. Trans. R. Soc. A* **2019**, *377*, 20180050. [CrossRef] [PubMed]
17. Ebisuzaki, T.; Miyahara, H.; Kataoka, R. Explosive volcanic eruptions triggered by cosmic rays: Volcano as a bubble chamber. *Gondwana Res.* **2011**, *19*, 1054–1061. [CrossRef]
18. Oláh, L.; Tanaka, H.K.M. Machine learning with muographic images as input: An application to volcano eruption forecasting. In *Muography: Exploring Earth's Subsurface with Elementary Particles*; AGU Publications: Malden, MA, USA, 2022; pp. 43–54. [CrossRef]
19. Tanaka, H. Muography for a dense tide monitoring network. *Sci. Rep.* **2022**, *12*, 6725. [CrossRef]
20. Gómez, H. Muon tomography using micromegas detectors: From Archaeology to nuclear safety applications. *Nucl. Instrum. Methods Phys. Res. Sect. A Accel. Spectrometers Detect. Assoc. Equip.* **2019**, *936*, 14–17. [CrossRef]
21. Berns, H.; Burnett, T.; Gran, R.; Wilkes, R. GPS time synchronization in school-network cosmic ray detectors. *IEEE Trans. Nucl. Sci.* **2004**, *51*, 848–853. [CrossRef]

22. Tanaka, H. Cosmic time synchronizer (CTS) for wireless and precise time synchronization using extended air showers. *Sci. Rep.* **2022**, *12*, 7078. [CrossRef]
23. Morishima, K.; Kuno, M.; Nishio, A.; Kitagawa, N.; Manabe, Y.; Moto, M.; Takasaki, F.; Fujii, H.; Satoh, K.; Kodama, H.; et al. Discovery of a big void in Khufu's Pyramid by observation of cosmic-ray muons. *Nature* **2017**, *552*, 386–390. [CrossRef]
24. Su, N.; Liu, Y.-Y.; Wang, L.; Cheng, J.-P. Muon radiography simulation for underground palace of Qinshihuang Mausoleum. *Acta Phys. Sin.* **2021**, *71*, 330–336. [CrossRef]
25. Liu, G.; Luo, X.; Tian, H.; Yao, K.; Niu, F.; Jin, L.; Gao, J.; Rong, J.; Fu, Z.; Kang, Y.; et al. High-precision muography in archaeogeophysics: A case study on Xi'an defensive walls. *J. Appl. Phys.* **2023**, *133*, 014901. [CrossRef]
26. Tanaka, H.; Bozza, C.; Bross, A.; Cantoni, E.; Catalano, O.; Cerretto, G.; Giammanco, A.; Gluyas, J.; Gnesi, I.; Holma, M.; et al. Muography. *Nat. Rev. Methods Primers* **2023**, *3*, 88. [CrossRef]
27. Tanaka, H. Muometric positioning system (μPS) with cosmic muons as a new underwater and underground positioning technique. *Sci. Rep.* **2020**, *10*, 18896. [CrossRef] [PubMed]
28. Tanaka, H. Wireless muometric navigation system. *Sci. Rep.* **2022**, *12*, 10114. [CrossRef]
29. Tanaka, H.; Gallo, G.; Gluyas, J.; Kamoshida, O.; Lo Presti, D.; Shimizu, T.; Steigerwald, S.; Takano, K.; Yang, Y.; Yokota, Y.; et al. First navigation with wireless muometric navigation system (MuWNS) in indoor and underground environments. *iScience* **2023**, *26*, 107000. [CrossRef]
30. Tanaka, H. Muometric positioning system (muPS) utilizing direction vectors of cosmic-ray muons for wireless indoor navigation at a centimeter-level accuracy. *Sci. Rep.* **2023**, *13*, 15272. [CrossRef]
31. Tanaka, H. Cosmic-ray arrival time (CAT) indoor navigation in the World Geodetic System. *Res. Square.* **2024**, preprint. [CrossRef]
32. Varga, D.; Tanaka, H. Developments of a centimeter-level precise muometric wireless navigation system (MuWNS-V) and its first demonstration using directional information from tracking detectors. *Sci. Rep.* **2024**, *14*, 7605. [CrossRef]
33. Xiong, K.; Wei, C.; Zhou, P. Research on underwater positioning method based on cosmic muons detection. *Tactical Missile Technol.* **2023**, *4*, 56–68. [CrossRef]
34. Yang, Y.; Ren, X. Muometric navigation with cosmic muon-ray. *J. Navig. Position.* **2023**, *11*, 8–13. [CrossRef]
35. Li, H.; Zhang, C.; Fan, X.; Tian, L.; Li, T.; Pang, Y.; Yang, Y. A muon high-resolution pseudorange measurement method: Application to muon navigation in confined spaces. *Chin. J. Aeronaut.* **2024**, *37*, 391–404. [CrossRef]
36. Wang, Y.; Liu, J.; Yang, L.; Zeng, Z.; Ma, H.; Yue, Q. Jinping Underground Laboratory and Rare Physics Experiments in China. *Nucl. Tech.* **2023**, *46*, 173–181. [CrossRef]
37. Bonomi, G.; Checchia, P.; D'Errico, M.; Pagano, D.; Saracino, G. Applications of cosmic-ray muons. *Prog. Part. Nucl. Phys.* **2020**, *112*, 103768. [CrossRef]
38. Agafonova, N.; Alexandrov, A.; Anokhina, A.; Aoki, S.; Ariga, A.; Ariga, T.; Bertolin, A.; Bozza, C.; Brugnera, R.; Buonaura, A.; et al. Measurement of the cosmic ray muon flux seasonal variation with the OPERA detector. *J. Cosmol. Astropart. Phys.* **2019**, *2019*, 003. [CrossRef]
39. Enqvist, T.; Mattila, A.; Föhr, V.; Jämsén, T.; Lehtola, M.; Narkilahti, J.; Joutsenvaara, J.; Nurmenniemi, S.; Peltoniemi, J.; Remes, H.; et al. Measurements of muon flux in the Pyhäsalmi underground laboratory. *Nucl. Instrum. Methods Phys. Res. Sect. A Accel. Spectrometers Detect. Assoc. Equip.* **2005**, *554*, 286–290. [CrossRef]
40. Bergamasco, L.; Bilokon, H.; Piazzoli, B.; Mannocchi, G.; Castagnoli, C.; Picchi, P. Deep underground multiple muons at the Mt. Blanc station. *Nuovo C. Lett.* **1979**, *26*, 609–614. [CrossRef]
41. Guo, Z.; Bathe-Peters, L.; Chen, S.; Chouaki, M.; Dou, W.; Guo, L.; Hussain, G.; Li, J.-J.; Liu, Q.; Luo, G.; et al. Muon flux measurement at china jinping underground laboratory. *Chin. Phys. C* **2021**, *45*, 025001. [CrossRef]
42. Stockel, C.T. A study of muons deep underground. I. Angular distribution and vertical intensity. *J. Phys. A Gen. Phys.* **1969**, *2*, 639. [CrossRef]
43. Gray, F.; Ruybal, C.; Totushek, J.; Mei, D.-M.; Thomas, K.; Zhang, C. Cosmic ray muon flux at the Sanford Underground Laboratory at Homestake. *Nucl. Instrum. Methods Phys. Res. Sect. A Accel. Spectrometers Detect. Assoc. Equip.* **2011**, *638*, 63–66. [CrossRef]
44. Esch, E.; Bowles, T.; Hime, A.; Pichlmaier, A.; Reifarth, R.; Wollnik, H. The cosmic ray muon flux at WIPP. *Nucl. Instrum. Methods Phys. Res. Sect. A Accel. Spectrometers Detect. Assoc. Equip.* **2005**, *538*, 516–525. [CrossRef]
45. Zhang, C.; Mei, D. Measuring muon-induced neutrons with liquid scintillation detector at Soudan mine. *Phys. Rev. D* **2014**, *90*, 122003. [CrossRef]
46. Robinson, M.; Kudryavtsev, V.A.; Lüscher, R.; McMillan, J.E.; Lightfoot, P.K.; Spooner, N.J.C.; Smith, N.J.T.; Liubarsky, I. Measurements of muon flux at 1070m vertical depth in the Boulby underground laboratory. *Nucl. Instrum. Methods Phys. Res. Sect. A Accel. Spectrometers Detect. Assoc. Equip.* **2003**, *511*, 347–353. [CrossRef]
47. Bellini, G.; Benziger, J.; Bick, D.; Bonfini, G.; Bravo, D.; Buizza Avanzini, M.; Caccianiga, B.; Cadonati, L.; Calaprice, F.; Carraro, C.; et al. Cosmic-muon flux and annual modulation in Borexino at 3800 m water-equivalent depth. *J. Cosmol. Astropart. Phys.* **2012**, *2012*, 015. [CrossRef]

48. Cherry, M.; Deakyne, M.; Lande, K.; Lee, C.K.; Steinberg, R.I.; Cleveland, B.; Fenyves, E.J. Multiple muons in the Homestake underground detector. *Phys. Rev. D Part. Fields Gravit. Cosmol./Phys. Rev. D Part. Fields* **1983**, *27*, 1444–1447. [CrossRef]
49. Formaggio, J. Measurement of Atmospheric Neutrinos at the Sudbury Neutrino Observatory. *Nucl. Phys. Sect. A* **2009**, *827*, 498c–500c. [CrossRef]
50. Mei, D.; Hime, A. Muon-induced background study for underground laboratories. *Phys. Rev. D—Part. Fields Gravit. Cosmol.* **2006**, *73*, 053004. [CrossRef]
51. Fedynitch, A.; Woodley, W.; Piro, M.C. On the accuracy of underground muon intensity calculations. *Astrophys. J.* **2022**, *928*, 27. [CrossRef]
52. Bonechi, L.; Bongi, M.; Fedele, D.; Grandi, M.; Ricciarini, S.; Vannuccini, E. Development of the ADAMO detector: Test with cosmic rays at different zenith angles. In Proceedings of the 29th International Cosmic Ray Conference, Pune, India, 3–10 August 2005; pp. 283–286.
53. Heck, D.; Knapp, J.; Capdevielle, J.N.; Schatz, G.; Thouw, T. *CORSIKA: A Monte Carlo Code to Simulate Extensive Air Showers*; Forschungszentrum Karlsruhe GmbH: Karlsruhe, Germany, 1998.
54. Gaisser, T.; Ralph, E.; Elisa, R. *Cosmic Rays and Particle Physics*; Cambridge University Press: Cambridge, UK, 1990.
55. Tang, A.; Horton-Smith, G.; Kudryavtsev, V.; Tonazzo, A. Muon simulations for super-kamiokande, kamland, and chooz. *Phys. Rev. D—Part. Fields Gravit. Cosmol.* **2006**, *74*, 053007. [CrossRef]
56. Bugaev, E.; Misaki, A.; Naumov, V.; Sinegovskaya, T.S.; Sinegovsky, S.I.; Takahashi, N. Atmospheric muon flux at sea level, underground, and underwater. *Physical Review D* **1998**, *58*, 054001. [CrossRef]
57. Pagano, D.; Bonomi, G.; Donzella, A.; Zenoni, A.; Zumerle, G.; Zurlo, N. EcoMug: An Efficient Cosmic Muon Generator for cosmic-ray muon applications. *Nucl. Instrum. Methods Phys. Res. Sect. A Accel. Spectrometers Detect. Assoc. Equip.* **2021**, *1014*, 165732. [CrossRef]
58. Woodley, W.; Fedynitch, A.; Piro, M.C. Cosmic ray muons in laboratories deep underground. *Phys. Rev. D* **2024**, *110*, 063006. [CrossRef]
59. Procureur, S. Muon imaging: Principles, technologies and applications. *Nucl. Instrum. Methods Phys. Res. Sect. A Accel. Spectrometers Detect. Assoc. Equip.* **2018**, *878*, 169–179. [CrossRef]
60. Li, Y.; Wang, G.; Xu, X.; Feng, L.; Wang, C. Geophysical application of cosmic-ray muon detection technology. *Prog. Geophys.* **2021**, *36*, 0753–0758. [CrossRef]
61. Bethe, H. Zur Theorie des Durchgangs schneller Korpuskularstrahlen durch Materie. *Ann. Der Phys.* **1930**, *397*, 325–428. [CrossRef]
62. Tanabashi, M.; Hagiwara, K.; Hikasa, K.; Nakamura, K.; Sumino, Y.; Takahashi, F.; Tanaka, J.; Agashe, K.; Alielli, G.; Amsler, C.; et al. Review of Particle Physics: Particle data groups. *Phys. Rev. D* **2018**, *98*, 1–1898. [CrossRef]
63. Groom, D.E.; Mokhov, N.V.; Striganov, S.I. Muon stopping power and range tables 10 MeV–100 TeV. *At. Data Nucl. Data Tables* **2001**, *78*, 183–356. [CrossRef]
64. Ye, B.; Li, Y.; Zhou, Z. Muon imaging and elemental analysis. *Physics* **2021**, *50*, 248–256. [CrossRef]
65. Wang, J.; Bu, Z.; Wang, Z.; Xu, J.; Zhou, L.; Zheng, Q. A High Precision Time Measurement Method Based on Phase-Fitting for Muon Detection. *arXiv* **2024**, arXiv:2411.08408.
66. Augusto, C.; Navia, C.; Lopes do Valle, R.; da Silva, T.F. Digital signal processing for time of flight measurements of muons at sea level. *Nucl. Instrum. Methods Phys. Res. Sect. A Accel. Spectrometers Detect. Assoc. Equip.* **2009**, *612*, 212–217. [CrossRef]
67. Niwase, T.; Wada, M.; Schury, P.; Haba, H.; Ishizawa, S.; Ito, Y.; Kaji, D.; Kimura, S.; Miyatake, H.; Morimoto, K.; et al. Development of an "α-TOF" detector for correlated measurement of atomic masses and decay properties. *Nucl. Instrum. Methods Phys. Res. Sect. A Accel. Spectrometers Detect. Assoc. Equip.* **2020**, *953*, 163198. [CrossRef]
68. Chaber, P.; Domański, P.D.; Dąbrowski, D.; Ławryńczuk, M.; Nebeluk, R.; Plamowski, S.; Zarzycki, K. Digital Twins in the Practice of High-Energy Physics Experiments: A Gas System for the Multipurpose Detector. *Sensors* **2022**, *22*, 678. [CrossRef]
69. Sykora, T. ATLAS Forward Proton Time-of-Flight Detector: LHC Run2 performance and experiences. *J. Instrum.* **2020**, *15*, C10004. [CrossRef]
70. Bonechi, L.; D'Alessandro, R.; Giammanco, A. Atmospheric muons as an imaging tool. *Rev. Phys.* **2020**, *5*, 100038. [CrossRef]
71. Teshima, N.; Aoki, M.; Higashino, Y.; Ikeuchi, H.; Komukai, K.; Nagao, D.; Nakatsugawa, Y.; Natori, H.; Seiya, Y.; Truong, N.M.; et al. Development of a multiwire proportional chamber with good tolerance to burst hits. *Nucl. Instrum. Methods Phys. Res. Sect. A Accel. Spectrometers Detect. Assoc. Equip.* **2021**, *999*, 165228. [CrossRef]
72. Shi, B.; Takahashi, H.; Yeom, J.; Takada, Y.; Hosono, Y.; Shimazoe, K.; Fujita, K. Characteristics of 16-channel ASIC preamplifier boareference detector for microstrip gas chamber and animal PET. *J. Nucl. Sci. Technol.* **2007**, *44*, 1356–1360. [CrossRef]
73. Xiong, J.; Zhou, R.; Pu, G.; Zhang, X.; Wang, Z.; Pu, Y. Development of multichannel readout electronics system for MWPC of heavy ion radiotherapy. *J. Instrum.* **2024**, *19*, T11011. [CrossRef]

74. Zadeba, E.A.; Vorobev, V.S.; Gazizova, D.V.; Kompaniets, K.G.; Miroshnichenko, E.A.; Nikolaenko, R.V.; Troshin, I.Y.; Khomchuk, E.P.; Shulzhenko, I.A.; Shutenko, V.V. Stand for Studying the Characteristics of Multiwire Drift Chambers. *Phys. At. Nucl.* **2025**, *87*, 1339–1347. [CrossRef]
75. Durham, J.M.; Poulson, D.; Bacon, J.; Chichester, D. L.; Guardincerri, E.; Morris, C. L.; Plaud-Ramos, K.; Schwendiman, W.; Tolman, J. D.; Winston, P. Verification of spent nuclear fuel in sealed dry storage casks via measurements of cosmic-ray muon scattering. *Phys. Rev. Appl.* **2018**, *9*, 044013. [CrossRef]
76. Morris, C.L.; Alexander, C.C.; Bacon, J.D.; Borozdin, K.N.; Clark, D.J.; Chartrand, R.; Espinoza, C.J.; Fraser, A.M.; Galassi, M.C.; Green, J.A.; et al. Tomographic imaging with cosmic ray muons. *Sci. Glob. Secur.* **2008**, *16*, 37–53. [CrossRef]
77. Ancius, D.; Aymanns, K.; Checchia, P.; Gonella, F.; Jussofie, A.; Montecassiano, F.; Murtezi, M.; Schwalbach, P.; Schoop, K.; Vanini, S.; et al. Modelling of safeguards verification of spent fuel dry storage casks using muon trackers. In Proceedings of the 41th ESARDA Symposium, Stresa, Italy, 14−16 May 2019; pp. 142–148.
78. He, W.; Xiao, S.; Shuai, M.; Chen, Y.; Lan, M.; Wei, M.; An, Q.; Lai, X. A grey incidence algorithm to detect high-Z material using cosmic ray muons. *J. Instrum.* **2017**, *12*, P10019. [CrossRef]
79. Olaáh, L.; Hamar, G.; Miyamoto, S.; Tanaka, H.K.M.; Varga, D. The first prototype of an MWPC-based borehole-detector and its application for muography of an underground pillar. *BUTSURI-TANSA (Geophys. Explor.)* **2018**, *71*, 161–168. [CrossRef]
80. Checchia, P.; Benettoni, M.; Bettella, G.; Conti, E.; Cossutta, L.; Furlan, M.; Gonella, F.; Klinger, J.; Montecassiano, F.; Nebbia, G.; et al. INFN muon tomography demonstrator: Past and recent results with an eye to near-future activities. *Philos. Trans. R. Soc. A: Math. Phys. Eng. Sci.* **2018**, *377*, 20180065. [CrossRef]
81. Anghel, V.; Armitage, J.; Botte, J.; Boudjemline, K.; Bueno, J.; Bryman, D.; Charles, E.; Cousins, T.; Drouin, P.-L.; Erlandson, A.; et al. Performance of a drift chamber candidate for a cosmic muon tomography system. *AIP Conf. Proc.* **2011**, *1412*, 129–136. [CrossRef]
82. Borisov, A.; Bogolyubskii, M.; Bozhko, N.; Isaev, A.N.; Kozhin, A.S.; Kozelov, A.V.; Plotnikov, I.S.; Sen'ko, V.A.; Soldatov, M.M.; Fakhrutdinov, R.M.; et al. A Muon Tomograph setup with a 3×3 m^2 area of overlapping. *Instrum. Exp. Tech.* **2012**, *55*, 151–160. [CrossRef]
83. Burns, J.; Quillin, S.; Stapleton, M.; Steer, C.; Snow, S. A drift chamber tracking system for muon scattering tomography applications. *J. Instrum.* **2015**, *10*, P10041. [CrossRef]
84. Baccani, G.; Bonechi, L.; Borselli, D.; Ciaranfi, R.; Cimmino, L.; Ciulli, V.; D'Alessandro, R.; Fratticioli, C.; Melon, B.; Noli, P.; et al. The MIMA project. Design, construction and performances of a compact hodoscope for muon radiography applications in the context of archaeology and geophysical prospections. *J. Instrum.* **2018**, *13*, P11001. [CrossRef]
85. Saracino, G.; Ambrosino, F.; Bonechi, L.; Bross, A.; Cimmino, L.; Ciaranfi, R.; D'Alessandro, R.; Giudicepietro, F.; Macedonio, G.; Martini, M.; et al. The MURAVES muon telescope: Technology and expected performances. *Ann. Geophys.* **2017**, *60*, S0103. [CrossRef]
86. Clarkson, A.; Hamilton, D.J.; Hoek, M.; Ireland, D.G.; Johnstone, J.R.; Kaiser, R.; Keri, T.; Lumsden, S.; Mahon, D.F.; McKinnon, B.; et al. GEANT4 simulation of a scintillating-fiber tracker for the cosmic-ray muon tomography of legacy nuclear waste containers. *Nucl. Instrum. Methods Phys. Res. Sect. A Accel. Spectrometers Detect. Assoc. Equip.* **2014**, *746*, 64–73. [CrossRef]
87. Zhai, J.; Tang, H.; Huang, X.; Liu, S.; Wang, Y.; Li, C.; Liang, X.; Zhang, Y.; Feng, M.; Zhang, Z.; et al. A high-position resolution trajectory detector system for cosmic ray muon tomography: Monte Carlo simulation. *Radiat. Detect. Technol. Methods* **2022**, *6*, 244–253. [CrossRef]
88. Gluyas, J.; Thompson, L.; Allen, D.; Benton, C.; Chadwick, P.; Clark, S.; Klinger, J.; Kudryavtsev, V.; Lincoln, D.; Maunder, B.; et al. Passive, continuous monitoring of carbon dioxide geostorage using muon tomography. *Philos. Trans. R. Soc. A Math. Phys. Eng. Sci.* **2018**, *377*, 20180059. [CrossRef]
89. Anastasio, A.; Ambrosino, F.; Basta, D.; Bonechi, L.; Brianzi, M.; Bross, A.; Callier, S.; Cassese, F.; Castellini, G.; Ciaranfi, R.; et al. The MU-RAY experiment: An application of SiPM technology to the understanding of volcanic phenomena. *Nucl. Instrum. Methods Phys. Res. Sect. A Accel. Spectrometers Detect. Assoc. Equip.* **2013**, *718*, 134–137. [CrossRef]
90. Anghel, V.; Armitage, J.; Baig, F.; Boniface, K.; Boudjemline, K.; Bueno, J.; Charles, E.; Drouin, P.-L.; Erlandson, A.; Gallant, G.; et al. A plastic scintillator-based muon tomography system with an integrated muon spectrometer. *Nucl. Instrum. Methods Phys. Res. Sect. A Accel. Spectrometers Detect. Assoc. Equip.* **2015**, *798*, 12–23. [CrossRef]
91. Luo, X.; Wang, Q.; Qin, K.; Tian, H.; Fu, Z.; Zhao, Y.; Shen, Z.; Liu, H.; Fu, Y.; Liu, G.; et al. Development and commissioning of a compact Cosmic Ray Muon imaging prototype. *Nucl. Instrum. Methods Phys. Res. Sect. A Accel. Spectrometers Detect. Assoc. Equip.* **2022**, *1033*, 166720. [CrossRef]
92. Fallavollita, F. Aging phenomena and discharge probability studies of the triple-GEM detectors for future upgrades of the CMS muon high rate region at the HL-LHC. *Nuclear Inst. Methods Phys. Res. A* **2019**, *936*, 427–429. [CrossRef]
93. Wang, X.; Aleksan, R.; Angelis, Y.; Bortfeldt, J.; Brunbauer, F.; Brunoldi, M.; Chatzianagnostou, E.; Datta, J.; Dehmelt, K.; Fanourakis, G.; et al. A novel diamond-like carbon based photocathode for PICOSEC Micromegas detectors. *J. Instrum.* **2024**, *19*, P08010. [CrossRef]

94. Albayrak, I.; Aune, S.; Gayoso, C.; Baron, P.; Bültmann, S.; Charles, G.; Christy, M.E.; Dodge, G.; Dzbenski, N.; Dupré, R.; et al. Design, construction, and performance of the GEM based radial time projection chamber for the BONuS12 experiment with CLAS12. *Nucl. Instrum. Methods Phys. Res. Sect. A Accel. Spectrometers Detect. Assoc. Equip.* **2024**, *1062*, 169190. [CrossRef]
95. Arakcheev, A.; Aulchenko, V.; Kudashkin, D.; Shekhtman, L.; Tolochko, B.; Zhulanov, V. Development of a silicon microstrip detector with single photon sensitivity for fast dynamic diffraction experiments at a synchrotron radiation beam. *J. Instrum.* **2017**, *12*, C06002. [CrossRef]
96. Willkes, R.J. DUMAND and AMANDA: High Energy Neutrino Astrophysics. *arXiv* **1994**, arXiv:astro-ph/9412019.
97. Aynutdinov, V.; Balkanov, V.; Belolaptikov, I.; Bezrukov, L.; Borschov, D.; Budnev, N.; Chensky, A.; Danilchenko, I.; Davidov, Y.; Domogatsky, G.; et al. Search for a diffuse flux of high-energy extraterrestrial neutrinos with the NT200 neutrino telescope. *Astropart. Phys.* **2005**, *25*, 140–150. [CrossRef]
98. Abbasi, R.; Ackermann, M.; Adams, J.; Agarwalla, S.; Aguilar, J.; Ahlers, M.; Alameddine, J.-M.; Amin, N.M.B.; Andeen, K.; Anton, G.; et al. Refining the IceCube detector geometry using muon and LED calibration data. *arXiv* **2023**, arXiv:2308.05330v1.
99. Allakhverdyan, A.V.; Avrorin, D.A.; Avrorin, V.A.; Aynutdinov, V.M.; Bardačová, Z.; Belolaptikov, I.A.; Bondarev, E.A.; Borina, I.V.; Budnev, N.M.; Chadymov, V.A.; et al. Recent Results From the Baikal-GVD Neutrino Telescope. *Mosc. Univ. Phys. Bull.* **2025**, *79*, 210–219. [CrossRef]
100. Louis, B.S. Time, position and orientation calibration using atmospheric muons in KM3NeT. In Proceedings of the 38th International Cosmic Ray Conference, Nagoya, Japan, 26 July–3 August 2023.
101. Suzuki, Y. The Super-Kamiokande experiment. *Eur. Phys. J. C* **2019**, *79*, 1–18. [CrossRef]
102. Bhattacharjee, P.; Calore, F. Probing the Dark Matter Capture Rate in a Local Population of Brown Dwarfs with IceCube Gen 2 †. *Particles* **2024**, *7*, 489–501. [CrossRef]
103. Ye, Z.P.; Hu, F.; Tian, W.; Chang, Q.C.; Chang, Y.L.; Cheng, Z.S.; Gao, J.; Ge, T.; Gong, G.H.; Guo, J.; et al. A multi-cubic-kilometre neutrino telescope in the western Pacific Ocean. *arXiv* **2024**, arXiv:2207.04519. [CrossRef]
104. Checchia, P. Review of possible applications of cosmic muon tomography. *J. Instrum.* **2016**, *11*, C12072. [CrossRef]
105. Sun, R.; Wang, G.; Cheng, Q.; Fu, L.; Chiang, K.-W.; Hsu, L.-T.; Ochieng, W.Y. Improving GPS code phase positioning accuracy in urban environments using machine learning. *IEEE Internet Things J.* **2020**, *8*, 7065–7078. [CrossRef]
106. InsideGNSS. Muons Make the Alt-PNT Roster with Ability to Penetrate Rock, Buildings and Earth—And Act at High Latitude. 2021. Available online: https://insidegnss.com/muons-make-the-alt-pnt-roster-with-ability-to-penetrate-rock-buildings-and-earth-and-act-at-high-latitude/ (accessed on 14 September 2023).
107. Tanaka, H. Cosmicray arrival time indoor navigation. *Proc. R. Sociaety A* **2025**, *481*, 20240346. [CrossRef]
108. Lisa, D. DARPA Embarks on Muon Project to Enhance Defense, Scientific Capabilities. Available online: https://www.darpa.mil/news-events/2022-07-22 (accessed on 14 September 2023).
109. Fidalgo, J.; Melis, S.; Cezón, A. POSITRINO: Positioning, Navigation and Timing with Neutrino Particles. In Proceedings of the 33rd International Technical Meeting of the Satellite Division of The Institute of Navigation (ION GNSS+ 2020), Online, 21–25 September 2020; pp. 2533–2547. [CrossRef]
110. Prieto, J.F.; Melis, S.; Cezon, A.; Azaola, M.; Mata, F.J.; Prajanu, C.; Andreopoulos, C.; Barry, C.; Roda, M.; Vidal, J.T.; et al. Submarine Navigation using Neutrinos. *arXiv* **2022**, arXiv:2207.09231.
111. Borodacz, K.; Szczepański, C.; Popowski, S. Review and selection of commercially available IMU for a short time inertial navigation. *Aircr. Eng. Aerosp. Technol.* **2022**, *94*, 45–59. [CrossRef]
112. Vandenbroucke, J.; Bravo, S.; Karn, P.; Meehan, M.; Plewa, M.; Ruggles, T.; Schultz, D.; Peacock, J.; Simons, A.L. Detecting particles with cell phones: The Distributed Electronic Cosmic-ray Observatory. In Proceedings of the 34th International Cosmic Ray Conference, The Hague, The Netherlands, 30 July–6 August 2015.
113. Chilingarian, A.; Chilingaryan, S.; Zazyan, M. Cosmic Ray Navigation System (CRoNS) for Autonomous Navigation in GPS-Denied Environments. *arXiv* **2024**, arXiv:2406.18608.